AJEMA GLOBAL RESEARCH NETWORK

AMERICAN Journal of Engineering, Mechanics and Architecture
Volume 3, Issue 10, 2025 ISSN (E): 2993-2637

Optimization of a Reformed Methanol-Fueled HT-PEMFC-Based CCHP System Using a Multi-Objective Approach

Samah Mohammed Abed

Abstract: High-temperature proton exchange membrane fuel cell (HT-PEMFC) systems operating on reformed methanol present a viable solution for decentralized power generation, offering benefits in fuel flexibility, system compactness, and thermal integration. However, optimizing their performance remains challenging due to the intricate coupling of thermochemical and heat recovery processes across multiple subsystems. In this study, an integrated combined cooling, heating, and power (CCHP) system is developed by thermally linking a reformed methanol HT-PEMFC with a double-effect LiBr–H_2O absorption refrigeration cycle. To maximize performance, a multi-objective optimization framework is established using the Non-Dominated Sorting Genetic Algorithm II (NSGA-II), targeting three conflicting objectives: maximizing exergy efficiency, minimizing exergy cost per unit product, and reducing specific CO_2 emissions. From the resulting Pareto-optimal set, the Technique for Order Preference by Similarity to Ideal Solution (TOPSIS) is applied to identify the most balanced operating scenario. The optimal solution achieves an exergy efficiency of 43.12%, a CO_2 emission rate of 0.510 kg/kWh, and an exergy cost of 167.59 USD/GJ—representing respective improvements of 20.73%, 17.10%, and 1.07% compared to a baseline configuration. The recommended operating ranges for critical parameters include a stack temperature of 173.94–179.91°C, a steam-to-carbon ratio of 1.78–1.80, a current density between 0.20–0.40 A/cm², and cathode stoichiometry from 2.29–2.52. These findings offer valuable insight into the design and operation of next-generation methanol-based tri-generation energy systems.

1. Introduction

Growing environmental concerns and the progressive depletion of fossil fuel reserves have catalyzed global efforts toward cleaner, more efficient energy technologies. Among the promising alternatives, hydrogen-powered systems—particularly proton exchange membrane fuel cells (PEMFCs)—have attracted significant attention for their low emissions and high conversion efficiency. While low-temperature PEMFCs (LT-PEMFCs) have already found applications in transportation, industry, and residential sectors, their reliance on ultra-high purity hydrogen poses major logistical and economic constraints, particularly in off-grid or mobile settings.

To overcome these limitations, high-temperature PEMFCs (HT-PEMFCs) have emerged as a robust alternative, offering several operational advantages including higher CO tolerance, simplified water management, and more effective thermal integration. One especially promising approach involves the use of reformed methanol as a hydrogen source, which eliminates the need for high-pressure hydrogen storage and enables in situ fuel processing. Methanol is a favorable candidate due to its liquid-state storage under ambient conditions, well-established reforming pathways, and compatibility with HT-PEMFC operating temperatures.

Recent research has demonstrated the technical feasibility and performance gains of methanol-reformed HT-PEMFC systems. For instance, increasing the stack temperature from 160°C to 180°C under controlled CO concentrations has been shown to boost cell voltage by up to 35%, while optimized system configurations have reported exergy efficiencies exceeding 50%. However, despite these advances, substantial energy losses—up to 45% of the input—remain unrecovered as waste heat, highlighting the need for integrated energy recovery strategies.

To address this, combined cooling, heating, and power (CCHP) systems have been proposed as a means to reclaim and utilize waste heat for auxiliary functions such as space conditioning or refrigeration. Absorption refrigeration cycles (ARCs), particularly double-effect LiBr–H_2O systems, are well-suited for coupling with HT-PEMFCs due to their ability to operate at the high-temperature levels associated with fuel cell exhaust.

Several studies have explored such configurations. Gwak et al. (2019) modeled a tri-generation system coupling a HT-PEMFC with an absorption chiller, highlighting the interplay between electrical and thermal outputs under varying load profiles. More recently, Ma et al. (2024) examined a methanol-fueled HT-PEMFC integrated with an ammonia-based absorption power refrigeration cycle (APRC), demonstrating the potential for exergy efficiencies above 56% under optimized conditions. However, the majority of existing literature has focused on single-objective assessments—prioritizing either thermodynamic, economic, or environmental performance in isolation.

In contrast, the present study proposes a holistic optimization framework for a thermally integrated HT-PEMFC-based CCHP system. By employing a multi-objective optimization approach, this research aims to concurrently evaluate and enhance system efficiency, carbon footprint, and economic viability under realistic operational constraints. The system model includes a reformed methanol HT-PEMFC and a double-effect LiBr–H_2O absorption chiller thermally coupled via a high-performance heat transfer fluid. A combination of NSGA-II and TOPSIS is used to identify optimal operating regimes, providing a comprehensive roadmap for next-generation tri-generation systems

Modeling Approach

The numerical modeling of the integrated CCHP system is conducted within the MATLAB environment (version R2021b), utilizing thermophysical property data primarily sourced from the open-source CoolProp library (Bell et al., 2014). While CoolProp provides robust property datasets for a range of pure fluids and refrigerant mixtures, it lacks the capability to dynamically resolve properties of LiBr–H_2O solutions across varying concentrations, which is a critical requirement for simulating double-effect absorption refrigeration cycles.

To address this limitation, the thermodynamic and transport properties of lithium bromide–water mixtures—including saturation pressure, density, specific enthalpy, entropy, and isobaric heat capacity—are instead calculated using well-established empirical correlations from the literature (Pátek & Klomfar, 2006; Wagner & Prüss, 2002). These correlations, which enable accurate evaluation over a broad range of temperatures and concentrations, are fully documented in the Supplementary Materials accompanying this study.

To maintain model tractability and ensure alignment with prior analytical frameworks, the following simplifying assumptions are adopted, consistent with established methodologies in comparable studies (e.g., Sarabchi et al., 2019; Xie et al., 2023):

1. Steady-state operation is assumed for all system components, with no temporal variations in state variables.
2. Complete thermal exchange is assumed between subsystems, whereby all waste heat is recovered and transferred through the heat transfer fluid loop (Therminol VP-1).

3. Chemical equilibrium is presumed for both the methanol steam reforming reactions and electrochemical processes within the fuel cell.
4. Ideal gas behavior is assumed for all gaseous streams involved in reforming, combustion, and fuel cell operation.
5. Complete oxidation of residual fuel is assumed in the burner, with no unburnt hydrocarbons or intermediates in the exhaust.

Reference Correlations for LiBr–H_2O Thermophysical Properties

To enable accurate modeling of the absorption refrigeration subsystem, property correlations developed by Pátek and Klomfar (2006) are implemented. These provide explicit functional forms for key thermophysical properties as a function of solution temperature and lithium bromide mass fraction, with validated applicability across the range of 273–500 K and concentrations up to approximately 75 wt.%. The model yields high computational efficiency and suitable accuracy for system-level simulations.

Reported uncertainties associated with the correlations include:

- ✓ ±0.5% for solution density
- ✓ ±2.1% for vapor pressure
- ✓ ±2.0% for specific heat capacity
- ✓ Approximately ±10 kJ/kg for specific enthalpy

These correlations are particularly advantageous for dynamic simulation of the double-effect ARC, as they support variable-concentration modeling across multiple pressure levels—a necessity for capturing the thermodynamic behavior of the generator, absorber, and solution heat exchangers under realistic operating conditions

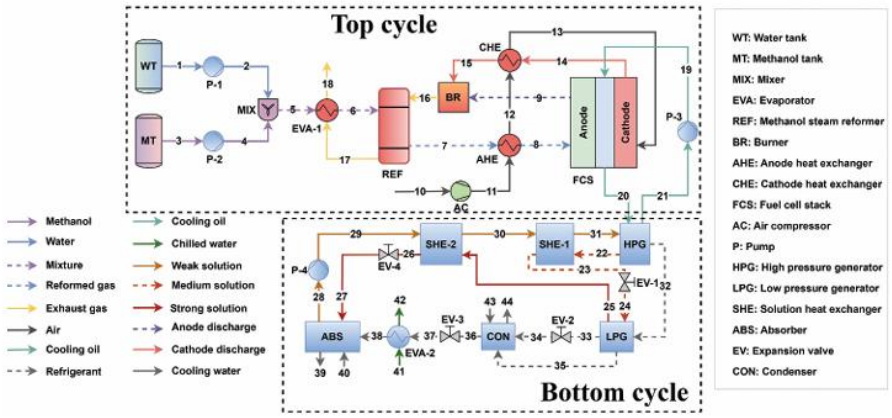

Figure 1. ***Schematic representation of the integrated RM HT-PEMFC and double-effect absorption refrigeration cycle (ARC).***

The reforming subsystem represents a critical component of the overall configuration, as its hydrogen production rate directly governs the electrical output of the HT-PEMFC stack and has a significant impact on the system's thermodynamic efficiency and economic viability. To accurately quantify the molar composition of the reformate gas—comprising H_2, CO, CO_2, H_2O, unconverted CH_3OH, and trace species—a chemical equilibrium approach based on Gibbs free energy minimization is employed.

This method determines the thermodynamically stable product distribution at specified temperature and pressure conditions by minimizing the system's total Gibbs free energy subject to atomic balance constraints. The necessary thermodynamic parameters and species-specific regression coefficients (e.g., for H_2, CO, CO_2, H_2O, CH_3OH) are sourced from established references and tabulated in Table S1 of the Supplementary Material.

Under the operating regime of interest, methanol steam reforming (MSR) constitutes the dominant reaction pathway:

These reactions proceed simultaneously within the reformer, and their relative extents are governed by the reactor temperature, pressure, and steam-to-carbon (S/C) ratio. As reported by Zhu et al. (2020), optimizing these operating parameters is essential for enhancing hydrogen yield while minimizing carbon monoxide concentration, thereby reducing anode overpotential and improving fuel cell performance

$$CH_3OH + H_2O \leftrightarrow CO_2 + 3H_2 \quad (1)$$

$$CO + H_2O \leftrightarrow CO_2 + H_2 \quad (2)$$

$$CH_3OH \leftrightarrow CO + 2H_2 \quad (3)$$

High-Temperature Proton Exchange Membrane Fuel Cell (HT-PEMFC) Module

The electrochemical performance of the HT-PEMFC subsystem is evaluated using a physics-based model grounded in the methodology introduced by Korsgaard et al. (2006). This model captures key voltage losses—including activation, ohmic, and concentration overpotentials—while accounting for temperature-dependent electrochemical kinetics and material properties. The stack output voltage is computed as a function of current density, operating temperature, gas partial pressures, and membrane conductivity. This modeling approach enables the estimation of net power output, thermal efficiency, and exergy performance under varying operational scenarios.

Double-Effect LiBr–H_2O Absorption Refrigeration Cycle (ARC) Module

The mathematical formulation of the double-effect LiBr–H_2O absorption refrigeration subsystem is developed through a component-level application of mass, species, and energy conservation laws. The model resolves steady-state mass flow and species transport across all major components—including the high- and low-pressure generators, condensers, evaporators, absorbers, and solution heat exchangers.

Energy balances are constructed based on the First and Second Laws of Thermodynamics, with enthalpy flows evaluated at each inlet and outlet stream. Irreversibilities within components are captured through entropy generation calculations, enabling exergy analysis alongside thermal performance evaluation. The model accommodates variable lithium bromide concentrations, heat source temperatures, and internal pressure levels, providing an accurate representation of the thermodynamic behavior under realistic coupling with the HT-PEMFC waste heat stream

$$\sum \dot{m}_{out} = \sum \dot{m}_{in} \quad (4)$$

$$\sum \dot{m}_{out} X_{out} = \sum \dot{m}_{in} X_{in} \quad (5)$$

$$W + Q + \sum \dot{m}_{in} h_{in} = \sum \dot{m}_{out} h_{out} \quad (6)$$

$$W = \dot{m}_f (h_{out} - h_{in}) = \dot{m}_f \left(h_{out,iso} - h_{in}\right) / \eta_{iso} \quad (7)$$

The heat exchanger areas are calculated as follows (Kiwan and Radaideh 2020):

$$Q = U \times A \times LMTD = \dot{m}_f (h_{in} - h_{out}) = \dot{m}_w (h_{in} - h_{out}) \quad (8)$$

$$LMTD = \frac{\Delta t_{\max} - \Delta t_{\min}}{\ln\left(\frac{\Delta t_{\max}}{\Delta t_{\min}}\right)} \quad (9)$$

System Modeling and Performance Evaluation

Within the present model, the logarithmic mean temperature difference (LMTD) method is employed to quantify the rate of heat transfer across heat exchanger surfaces, where AAA represents the effective heat transfer area and UUU denotes the overall heat transfer coefficient. The complete computational framework governing the double-effect LiBr–H_2O absorption refrigeration cycle (ARC) is illustrated in Figure S1 of the Supplementary Material.

The primary governing equations for the methanol steam reformer, the double-effect absorption cycle, and the high-temperature PEM fuel cell (HT-PEMFC) are systematically summarized in Table 1. All variables and parameters referenced in these equations are explicitly defined in the Nomenclature section, with additional clarification provided in footnotes where appropriate. Empirical correlations and assigned values for the heat transfer coefficients associated with individual system components are listed in Table 2.

Performance Assessment Methodology

A comprehensive performance analysis is undertaken to evaluate the proposed integrated system from thermodynamic, environmental, and economic perspectives. The analytical formulations used in these evaluations are consolidated in Table 3, which includes expressions for exergy efficiency, specific CO_2 emissions, and cost-based metrics.

Furthermore, the methodology for estimating capital and operating costs of major components is detailed in Table 4, including standardized cost functions for purchased equipment and a breakdown of cost contributions across subsystems. This multi-dimensional assessment enables a holistic appraisal of system feasibility and facilitates informed optimization of operating parameters

Table 1. The equations for the MSR, HT-PEMFC, and double-effect ARC models.

Model	Governing equations[a]	Eq.
MSR model		
Gibbs free energy minimization	$\min_{n_i}(G^t)_{T,P}=\sum_{i=1}^{C} n_i\bar{G}_i=\sum_{i=1}^{C} n_i\cdot(G_i^0+R\cdot T\cdot \ln\frac{\bar{f}_i}{f_i^0})$	(10)
Elemental balance	$\sum_j n_j\cdot a_{ik}-A_k=0$	(11)
HT-PEMFC model		
Voltage of the single cell	$U_{cell}=U_0-V_a-V_c-V_{ohmic}$	(12)
Anode overpotential	$V_a=\frac{R\cdot T_{FC}}{\alpha_{an}\cdot F}\cdot \operatorname{arcsinh}\left(\frac{i}{2\cdot k_{eh}\cdot\theta_{H_2}}\right)$	(13)
	$\rho\frac{d\theta_{H_2}}{dt}=0=k_{fh}\cdot x_{H_2}\cdot p\cdot[1-\theta_{H_2}-\theta_{CO}]^2-b_{fh}\cdot k_{fh}\cdot\theta_{H_2}^2-i$	(14)
	$\rho\frac{d\theta_{CO}}{dt}=0=k_{fc}\cdot x_{CO}\cdot p\cdot[1-\theta_{H_2}-\theta_{CO}]-b_{fc}\cdot k_{fc}\cdot\theta_{CO}-\frac{i\cdot k_{ec}\cdot\theta_{CO}}{2\cdot k_{eh}\cdot\theta_{H_2}}$	(15)
Cathode overpotential	$V_c=\frac{R\cdot T_{FC}}{4\cdot\alpha_c\cdot F}\cdot\ln\left(\frac{i_o+i}{i_o}\right)+\frac{R_{conc}\cdot i}{\lambda_{air}-1}$	(16)
	$\alpha_c=a_0\cdot T_{FC}+b_0$	(17)
	$i_o=a_3\cdot e^{-b_3\cdot T_{FC}}$	(18)
	$R_{conc}=a_2\cdot T_{FC}+b_2$	(19)
Ohmic overpotential	$V_{ohmic}=i\cdot R_{ohmic}$	(20)
	$R_{ohmic}=a_1\cdot T_{FC}+b_1$	(21)
Required hydrogen	$n_{H_2}=\frac{N_{cell}\cdot A_{cell}\cdot j}{u_f\cdot 2F}$	(22)
Required air	$n_{air}=\lambda_{air}\frac{N_{cell}\cdot A_{cell}\cdot j}{0.21\cdot 4F}$	(23)
Double-effect ARC model		
High-pressure generator	$Q_{HPG}=\dot{m}_{22}h_{22}+\dot{m}_{32}h_{32}-\dot{m}_{31}h_{31}=\dot{m}_{20}(h_{20}-h_{21})$	(24)
Solution heat exchanger-1	$Q_{SHE1}=\dot{m}_{30}(h_{31}-h_{30})=\dot{m}(h_{22}-h_{23})$	(25)
Solution heat exchanger-2	$Q_{SHE2}=\dot{m}_{29}(h_{30}-h_{29})=\dot{m}(h_{25}-h_{26})$	(26)
Low-pressure generator	$Q_{LPG}=\dot{m}_{25}h_{25}+\dot{m}_{35}h_{35}-\dot{m}_{24}h_{24}=\dot{m}_{32}(h_{32}-h_{33})$	(27)
Condenser	$Q_{CON}=\dot{m}_{34}h_{34}+\dot{m}_{35}h_{35}-\dot{m}_{36}h_{36}=\dot{m}_{43}(h_{44}-h_{43})$	(28)
Evaporator-2	$Q_{EVA2}=\dot{m}_{37}(h_{38}-h_{37})=\dot{m}_{41}(h_{41}-h_{42})$	(29)
Absorber	$Q_{ABS}=\dot{m}_{27}h_{27}+\dot{m}_{38}h_{38}-\dot{m}_{28}h_{28}=\dot{m}_{402}(h_{39}-h_{40})$	(30)
Expansion valves	$h_{23}=h_{24}$; $h_{33}=h_{34}$; $h_{36}=h_{37}$; $h_{26}=h_{27}$	(31)
Solution pump	$P_{SP}=\dot{m}_{28}(h_{29}-h_{28})$	(32)

Table 2. Heat transfer coefficients (kW/(m2·°C)) of each component in the proposed system (Sarabchi et al. 2019; Xie et al. 2023.).

Parameters	Value	Parameters	Value
U_{REF}	0.9	U_{EVA1}	1.6
U_{CHE}	1.0	U_{EVA2}	1.6
U_{HPG}	1.6	U_{AHE}	1.0
U_{SHE-1}	1.1	U_{LPG}	1.6
U_{ABS}	0.8	U_{SHE-2}	1.1
U_{CON}	1.0		

Table 3. Evaluation model for the proposed system.

Model	Governing equations[a]	Eq.
Exergy analysis		
Net output power	$P_{net}=P_{stack}-P_{AC}-P_{P1}-P_{P2}-P_{P3}-P_{P4}$	(33)
Total exergy of a particular stream	$\dot{E}x = \dot{E}x_{ph} + \dot{E}x_{ch}$	(34)
Physical exergy	$\dot{E}x_{ph} = \dot{m}.((h-h_0) - T_0.(S-S_0))$	(35)
Chemical exergy	$Ex_{ch}=n \cdot (\sum_i y_i \cdot ex_i^{ch.0} + R \cdot T_0 \sum_i y_i \cdot \ln y_i)$	(36)
Total exergy benefits	$\dot{E}x_{p,tot} = P_{net} + (\dot{E}x_{40} - \dot{E}x_{39}) + (\dot{E}x_{36} - \dot{E}x_{35})(\dot{E}x_{38} - \dot{E}x_{37})$	(37)
System exergy efficiency	$\eta_{Ex_{p,tot}} = \frac{\dot{E}x_{p,tot}}{\dot{n}_{CH3OH} \cdot \dot{e}_{ch,CH3OH}}$	(38)
Economic analysis		
CIOM cost rate	$\dot{Z}_k = (\frac{PEC_k \cdot CRF}{N_h} + \frac{PEC_k \cdot \varphi}{N_h}) \cdot \frac{CEPCI_{2022}}{CEPCI_0}$	(39)
Capital recovery factor	$CRF=\frac{i_r \cdot (1+i_r)^{N_y}}{(1+i_r)^{N_y}-1}$	(40)
Cost of unit damage of CO_2	$c_{CO_2}= 0.02086$ \$/kg	(41)
Cost of unit methanol	$c_{CH_3OH}= 24.69$ \$/GJ	(42)
Cost rate of CO_2 emissions	$\dot{C}_{CO_2} = \dot{m}_{CO_2} \cdot c_{CO_2}$	(43)
Cost rate of methanol	$\dot{C}_{fuel} = \dot{n}_{CH3OH} \cdot c_{CH3OH}$	(44)
Total cost rate	$\dot{C}_{total} = \dot{C}_{fuel} + \dot{Z}_{total} + \dot{C}_{CO_2}$	(45)
Exergy cost per unit product	$\dot{c}_{p,tot} = \frac{\dot{C}_{total}}{\dot{E}x_{p,tot}}$	(46)
Environmental analysis		
Specific CO_2 emissions	$sm_{co_2} = \frac{3600 \cdot \dot{m}_{co_2}}{\dot{E}x_{p,tot}}$	(47)

Table 4. Purchase equipment cost equations for each component (Haghghi et al. 2019; Sarabchi, Yari, and Seyed Mahmoudi 2021.).

Components	PEC equation	Year	$CEPCI_0$
Pump	$Z_{Pump} = 2100 \times (\frac{P_{Pump}}{10})^{0.26} \times (\frac{1-\eta_{Pump}}{\eta_{Pump}})^{0.6}$	2000	394.1
Evaporator	$Z_{EVA}= 16000 \times (\frac{A_{EVA}}{100})^{0.6}$	2000	394.1
Reformer	$Z_{REF}= (130 \times (\frac{A_{REF}}{0.093})^{0.78}) + 3240 \times (V_{REF})^{0.4} + 21280.5 \times V_{REF}$	1997	386.5
Burner	$Z_{BUR} = \frac{46.08 \times \dot{m}_{15}}{0.995 - \frac{P_{16}}{P_{15}}} \times (1 + \exp(0.018 \times T_{16} - 26.4))$	1994	368.1
AHE, CHE, SHE	$Z_{HE}= 130 \times (\frac{A_{HE}}{0.093})^{0.78}$	2005	468.2
HPG, LPG	$Z_{Generator}= 17500 \times (\frac{A_{Generator}}{100})^{0.6}$	2000	394.1
AC	$Z_{AC}= 91562 \times (\frac{P_{AC}}{455})^{0.67}$	2003	402.3
HT-PEMFC	$Z_{HT-PEMFC}= 1219.7 \times P_{HT-PEMFC}$	1998	389.5
Absorber	$Z_{ABS}= 16500 \times (\frac{A_{ABS}}{100})^{0.6}$	2000	394.1
Condenser	$Z_{CON}= 8000 \times (\frac{A_{CON}}{100})^{0.6}$	2000	394.1

Cost Normalization and Optimization Framework

To ensure consistency in economic assessment, all component cost estimates are normalized to a common base year (2022) using the Chemical Engineering Plant Cost Index (CEPCI), following the methodology outlined in Restelli et al. (2024). This adjustment facilitates reliable comparisons across cost data sourced from different studies or historical datasets.

Multi-Objective Optimization Approach

A tri-objective optimization framework is employed in this study, aiming to simultaneously optimize three critical and inherently conflicting performance indicators:

- ✓ System exergy efficiency (thermodynamic performance),
- ✓ Exergy cost per unit product (economic performance), and
- ✓ Specific CO_2 emissions (environmental impact).

The optimization problem is solved using the Non-Dominated Sorting Genetic Algorithm II (NSGA-II), a robust evolutionary algorithm well-suited for handling complex, nonlinear, and conflicting objective functions. NSGA-II is utilized to generate a Pareto front that encapsulates a set of non-dominated solutions, representing optimal trade-offs among the three competing objectives.

To identify the most favorable solution within the Pareto-optimal set, the Technique for Order Preference by Similarity to Ideal Solution (TOPSIS) is applied. This multi-criteria decision-making method evaluates the relative proximity of each Pareto solution to an ideal point (maximal exergy efficiency, minimal cost, and minimal emissions), under the assumption of equal weighting across all objectives.

The decision space—that is, the range of variables over which the optimization is performed—includes key operating parameters such as current density, stack temperature, steam-to-carbon ratio, and cathode stoichiometry. These parameters are varied within physically and operationally feasible bounds to ensure that the resulting optimal configurations are both practical and implementable.

$$\min F(x_k) = \min[f_1(x_k), f_2(x_k), f_3(x_k)] = \min\left(-\eta_{Ex,tot}, c_{p,tot}, sm_{CO_2}\right) \tag{48}$$

$$x_k = (x_1, x_2, x_3, x_4) = (i, T_{FC}, S/C, \lambda_{air}) \tag{49}$$

The lower and upper bounds for these operating parameters are drawn from the literature (Korsgaard et al., 2006; Patel & Pant, 2006; Sarabchi, Yari, & Seyed Mahmoudi, 2021). The flowchart for the NSGA-II optimization process is presented in Figure 2.

Validation

The model is validated through two primary comparisons with experimental and literature data:

- The polarization curve of a single HT-PEMFC cell is compared against data from Korsgaard et al. (2006) in Figure 3(a), and the results show close correspondence, indicating the model accurately predicts voltage vs. current density behavior
- Methanol conversion rates under identical operating conditions (steam-to-carbon ratio from 1.0 to 2.4, reforming temperature 160-300 °C, atmospheric pressure) are compared to literature results (Xing et al. 2020) in Figure 3(b). The model's predictions correlate strongly with the reference values, particularly at reforming temperatures above ~200 °C, confirming the accuracy of the methanol steam reforming (MSR) module.

If you want, I can try to retrieve more detailed numerical values from the cited studies (e.g. from Korsgaard et al., 2006 or Xing et al., 2020) to enrich your validation section

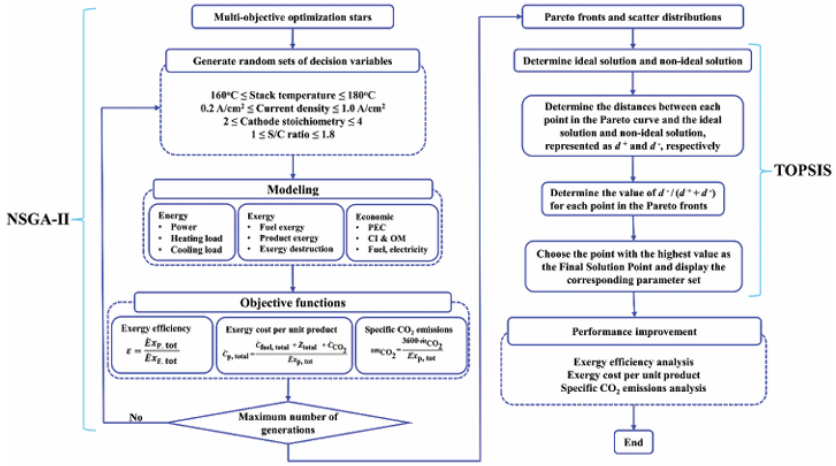

Figure 2. The technical roadmap of the proposed system in performance optimization

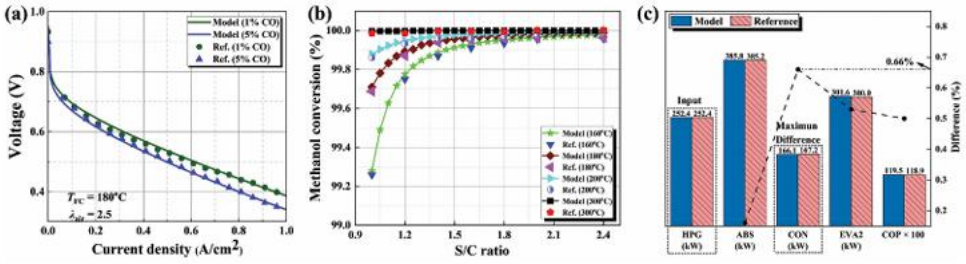

Figure 3. ***Model validation results for (a) HT-PEMFC, (b) Methanol Steam Reformer (MSR), and (c) Double-Effect Absorption Refrigeration Cycle (ARC).***

To ensure the reliability of the developed system model, validation was carried out under representative operating conditions as reported by Gomri and Hakimi (2008). In particular, Figure 3(c) compares the simulated outputs of the double-effect ARC with experimental or reference data, exhibiting a maximum relative deviation of only 0.66%. This minor discrepancy highlights the predictive accuracy and computational robustness of the model, thereby affirming its suitability for subsequent parametric and optimization analyses.

4. Results and Discussion

The results are presented in two major parts: (1) parametric analysis, and (2) multi-objective optimization. Prior to executing the optimization procedure, a comprehensive parametric study is conducted to understand how key operating variables affect system performance. This step is critical to identifying influential factors and establishing performance trends that guide the optimization phase.

4.1 Parametric Analysis

The parametric evaluation investigates the effects of four principal operating parameters on system-level performance metrics:

- ✓ Current density (j)
- ✓ Fuel cell stack temperature (TFC)(T_{\text{FC}})(TFC),
- ✓ Steam-to-carbon ratio (S/C)(\text{S/C})(S/C), and
- ✓ Cathode stoichiometry (λair)(\lambda_{\text{air}})(λair).

The corresponding performance indicators assessed are:

- ✓ Overall system exergy efficiency (ηEx,tot)(\eta_{\text{Ex,tot}})(ηEx,tot),
- ✓ Exergy cost per unit of useful output (cp,tot)(c_{p,\text{tot}})(cp,tot), and
- ✓ Specific CO_2 emissions (smCO₂)(sm_{\text{CO₂}})(smCO₂).

The baseline operating settings employed throughout the analysis are summarized in Table 5.

Current Density Effect

As illustrated in Figure 4(a), increasing the current density from 0.20 to 1.00 A/cm² results in a marked decrease in total exergy efficiency—from 43.37% to 28.97%. This decline is explained by the fact that the incremental exergy benefits derived from net electrical output, heat recovery, and cooling are outpaced by the growing exergy input associated with increased methanol consumption.

Economically, the exergy cost per unit output (cp,tot) follows a non-monotonic trend. It initially declines, reaching a minimum of 166.53 USD/GJ, before rising at higher current densities. This behavior occurs because the total cost rate—which includes capital investment, operating and maintenance (CIOM), fuel costs, and CO_2-related externalities—initially increases more slowly

than the total exergy benefits. However, beyond a certain point (approximately j = 0.40 A/cm²), the rate of cost increase overtakes the rate of exergy gain, leading to an upturn in cp,tot.

From an environmental perspective, the specific CO_2 emissions ($smCO_2$) rise steadily with increasing current density, climbing from 0.51 to 0.76 kg/kWh. This increase is attributed to higher fuel consumption and diminishing marginal efficiency at elevated current densities.

Parameters	Value	Parameters	Value
Ambient pressure, p_0	101.3 kPa	Isentropic efficiency of pumps	85%
Ambient temperature, T_0	25°C	Isentropic efficiency of AC	55%
Reference concentration of LiBr-H_2O solution	0.48	Reformer volume	0.0057 m^3
HT-PEMFC			
Number of cells, N_{cell}	120	Cathode stoichiometry, λ_{air}	2.5
Universal gas constant, R	8.314 J/(mol·K)	Fuel utilization ratio, u_f	0.8
Faraday constant, F	96485 C/mol	Active area, A_{cell}	0.03 m^2
Operating temperature, T_{FC}	180°C	Anode symmetry factor, a_{an}	0.5
Current density, j	0.6 A/cm^2	Open circuit voltage, U_0	0.95 V
Methanol steam reformer			
Reformer temperature, $T_{reformer}$	230°C	Steam to carbon ratio, S/C	1.3
Economic parameters			
Annual operation time, N_h	3650 hours	Lifetime, N_y	5 years
Interest rate, i_r	0.12	Maintenance factor, φ	0.06

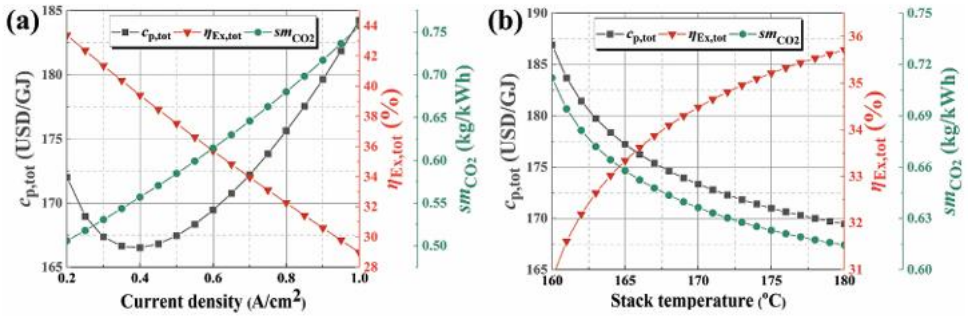

Figure 4. ***Influence of (a) current density and (b) stack temperature on integrated system performance.***

At a current density of 0.40 A/cm², the rates of increase for both the total cost rate and exergy gains become approximately equal, which explains the observed inflection point in the economic performance curve. From an environmental perspective, as current density (j) increases, specific CO_2 emissions ($smCO_2$) also rise—from 0.51 to 0.76 kg/kWh—due to increased fuel consumption and declining marginal efficiency at higher current loads.

Effect of Stack Temperature (TFC)(T_{\text{FC}})(TFC)

The upper thermal threshold for the high-temperature proton exchange membrane fuel cell (HT-PEMFC) stack, denoted as TFCT_{\text{FC}}TFC, is governed by the thermal stability of the polybenzimidazole (PBI) membrane. To prevent thermal degradation, operational guidelines recommend maintaining the stack temperature within 150°C to 200°C (Marandi, Sarabchi, and Yari, 2021). The influence of TFCT_{\text{FC}}TFC on system performance metrics is depicted in Figure 4(b).

From a thermodynamic standpoint, the overall system exergy efficiency (ηEx,tot)(\eta_{\text{Ex,tot}})(ηEx,tot) improves with increasing stack temperature. This enhancement primarily stems from the rise in net electrical output, which constitutes the dominant component of exergy gains, while the changes in thermal exergy (associated with heating and cooling) remain relatively minor. Higher TFCT_{\text{FC}}TFC values effectively reduce electrochemical losses, including both ohmic resistance and activation overpotentials at the anode and cathode, thereby boosting cell voltage and power output.

Economically, under a fixed current density and constant system scale, the fuel cost and CO_2-related damage cost remain invariant. However, the capital investment, operation, and maintenance (CIOM) cost rate increases more slowly than the corresponding exergy benefits,

resulting in a net decline in the exergy cost per unit product (cp,tot) with higher TFCT_{\text{FC}}TFC.

From an environmental perspective, elevated stack temperatures contribute to improved fuel utilization, thus lowering specific CO_2 emissions. As a result, smCO_2 decreases from 0.71 to 0.61 kg/kWh as TFCT_{\text{FC}}TFC increases across the evaluated range.

Effect of Steam-to-Carbon Ratio (S/C)(S/C)(S/C)

Raising the steam-to-carbon ratio (S/C) plays a crucial role in steering the reforming chemistry toward more favorable outcomes. Specifically, higher S/C values inhibit methanol decomposition reactions, thereby promoting hydrogen production and reducing carbon monoxide (CO) levels through the water-gas shift (WGS) reaction. This leads to improved yields of both H_2 and CO_2 (Qureshi et al., 2021). However, excessively high S/C ratios introduce thermal inefficiencies, primarily due to the increased energy demand for water vaporization.

Figure 5(a) illustrates how variations in S/C affect the three main performance metrics.

From a thermodynamic perspective, as S/C increases, the lower CO content reduces anode overpotential, which in turn raises the output voltage and net electrical power. This enhances the overall exergy benefit, reflected in a corresponding increase in system exergy efficiency (η\etaη).

Economically, for a constant current density, the total cost rate remains relatively stable. However, the rising exergy output with higher S/C values leads to a decline in cp,tot, indicating improved economic efficiency.

Environmentally, the reduction in CO emissions and the increase in exergy output result in lower specific CO_2 emissions. This is evidenced by the downward trend of the smCO_2 curve as S/C increases from 1.20 to 1.80.

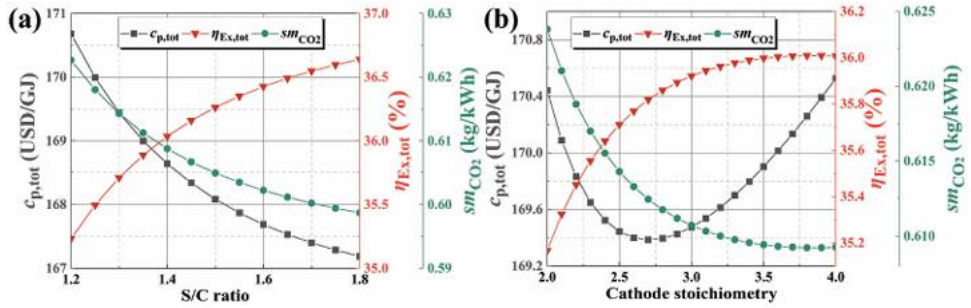

Figure 5. ***Effect of (a) Steam-to-carbon (S/C) ratio and (b) Cathode stoichiometry (λ_air) on system performance.***

Impact of Cathode Stoichiometry

As illustrated in Figure 5(b), the variation of cathode stoichiometry (λ_air) significantly affects the overall performance of the integrated system. From a thermodynamic perspective, increasing λ_air from 2.00 to 4.00 leads to a rise in total exergy efficiency ($\eta_{ex,tot}$) from 35.17% to 36.01%. This improvement is primarily due to the reduction in cathode-side activation losses, which enhances the effective cell voltage and increases the exergy output, assuming a constant fuel input at a fixed current density.

From an economic standpoint, the exergy cost per unit of useful product (cp_{tot}) initially declines, reaches a local minimum, and then rises as λ_air continues to increase. This trend is governed by the relative rates of change in total cost rate and exergy gains: at lower λ_air values, the system benefits from improved efficiency without proportional increases in cost, whereas at higher λ_air, the cost rate eventually outpaces the marginal exergy benefits, reversing the cost-effectiveness trend.

Environmentally, specific CO_2 emissions ($smCO_2$) exhibit a marginal decrease from 0.62 to 0.61 kg/kWh. This slight improvement is attributable to the continuous gain in total exergy output, which offsets emissions per unit of electricity delivered.

Multi-Objective Optimization

To assess and enhance system performance holistically, a tri-objective optimization framework is developed, targeting three distinct performance metrics:

- ✓ Thermodynamic criterion: Total exergy efficiency (ηEx,tot)(η_{\text{Ex,tot}})(ηEx,tot),
- ✓ Economic criterion: Exergy cost per unit product (cptot)(cp_{\text{tot}})(cptot),
- ✓ Environmental criterion: Specific CO_2 emissions (smCO2)($smCO_2$)(smCO2).

The Non-Dominated Sorting Genetic Algorithm II (NSGA-II) is applied to explore the multi-dimensional decision space and generate a set of Pareto-optimal solutions. The algorithm parameters used for the optimization process are detailed in Table 6.

Pareto Front Analysis

Figure 6(a) presents the distribution of the three-dimensional Pareto front, where the x-axis denotes $\eta_{ex,tot}$, the y-axis corresponds to cp_{tot}, and the z-axis represents $smCO_2$. The point with the highest exergy efficiency, 44.12%, is identified as Point B, while the minimum exergy cost (164.85 $/GJ) and lowest CO_2 emissions (0.497 kg/kWh) are located at Point A and Point B, respectively.

Figures 6(b) and 6(c) reveal clear trade-offs between the economic and thermodynamic objectives (cp_{tot} vs. $\eta_{ex,tot}$) and between the economic and environmental metrics (cp_{tot} vs. $smCO_2$). However, Figure 6(d) shows that $\eta_{ex,tot}$ and $smCO_2$ exhibit minimal conflict, indicating that improvements in efficiency also tend to reduce emissions.

Each point on the Pareto front reflects a non-dominated solution, balancing competing objectives without being outperformed across all criteria. To determine a single preferred solution, the Technique for Order Preference by Similarity to Ideal Solution (TOPSIS) is employed. This method ranks solutions based on their proximity to an idealized optimum, using normalized values and cosine similarity metrics.

The Final Optimal Point (FOP) selected through TOPSIS corresponds to:

- ✓ $\eta_{ex,tot} = 43.12\%$
- ✓ $cp_{tot} = 167.59$ $/GJ
- ✓ $smCO_2 = 0.510$ kg/kWh

Scatter Analysis of Decision Variables

A scatter distribution analysis of the Pareto front solutions provides insights into the optimal operational ranges for key parameters:

- ➢ Figure 7(a) identifies the optimal range for:
- ✓ Current density (j): 0.20 – 0.40 A/cm²
- ✓ Stack temperature (T_xFC): 173.94°C – 179.91°C
- ➢ Figure 7(b) shows the ideal range for:
- ✓ Cathode stoichiometry (λ_air): 2.29 – 2.52
- ✓ Steam-to-carbon ratio (S/C): 1.78 – 1.80

Based on this distribution, it can be inferred that maximizing system performance in the CCHP configuration involves:

- Elevating the stack temperature and steam-to-carbon ratio to enhance fuel conversion and exergy recovery,
- While maintaining low values of current density and cathode stoichiometry to reduce losses and optimize fuel utilization.

This strategic combination ensures thermodynamic efficiency, cost-effectiveness, and emission reduction, validating the viability of the proposed system architecture under optimized conditions

Table 6. Specifications for NSGA-II.

Parameters	Specification
Population size	100
Maximum generations	200
Pareto fraction Crossover fraction	0.8
Crossover fraction	0.8
Tournament size	2
Crossover function	Intermediate
Mutation function	Constraint dependent
Selection function	Tournament

Conclusions

This study presents a detailed multi-objective optimization analysis of an integrated combined cooling, heating, and power (CCHP) system comprising a methanol steam reformer, a high-temperature proton exchange membrane fuel cell (HT-PEMFC) stack, and a double-effect lithium bromide–water absorption refrigeration cycle. The optimization framework, based on the Non-Dominated Sorting Genetic Algorithm II (NSGA-II), was designed to concurrently enhance three key performance indicators: system exergy efficiency, exergy cost per unit of useful output, and specific CO_2 emissions. The final optimal operating point was selected from the resulting Pareto-optimal set using the Technique for Order Preference by Similarity to Ideal Solution (TOPSIS).

The decision variables optimized included current density, stack temperature, reformer operating temperature, and the steam-to-carbon (S/C) ratio. The Pareto front provided valuable insight into the interdependencies and trade-offs among the thermodynamic, economic, and environmental objectives.

The principal findings and insights derived from this study can be summarized as follows:

- Elevated stack temperatures and higher S/C ratios were found to have a strong positive influence on overall system performance. These parameters not only increased the system's exergy efficiency, but also led to reductions in both specific CO_2 emissions and the exergy cost per unit of product.
- The effect of increasing cathode stoichiometry revealed a nonlinear trend: while moderate increases improved exergy efficiency and reduced emissions, excessive values led to diminishing returns and a rise in the exergy cost, suggesting an optimal operating window.
- The multi-objective optimization framework effectively captured the balance between competing objectives. The optimal solution obtained via TOPSIS yielded:

✓ Exergy efficiency: 43.12%

✓ Specific CO_2 emissions: 0.510 kg/kWh

✓ Exergy cost: 167.59 USD/GJ

These figures represent an improvement of 20.73% in efficiency, and reductions of 17.10% and 1.07% in emissions and cost, respectively, relative to the reference scenario.

- The system demonstrated sensitivity to key operational boundaries, with optimal performance achieved by operating:

- ✓ The fuel cell stack temperature and S/C ratio near their upper bounds (173.94–179.91°C and 1.78–1.80, respectively),
- ✓ While maintaining current density and cathode stoichiometry closer to their lower bounds (0.20–0.40 A/cm² and 2.29–2.52, respectively).

This research establishes a comprehensive modeling and optimization platform for the development of advanced tri-generation systems based on reformed methanol-fed HT-PEMFCs. Moreover, the use of genetic algorithm-based multi-objective optimization offers practical guidance for improving integrated energy system design, particularly in contexts where simultaneous thermal, electrical, and cooling demands must be met with high efficiency and minimal environmental impact.

Looking ahead, further refinements—especially focused on the thermodynamic optimization of the condenser and absorber units within the double-effect absorption cycle—are recommended to unlock additional performance enhancements and improve the overall viability of such systems in real-world applications

References

1. Al-Tememy, M. G. H., and Y. Devrim. 2021.
2. Development of effective bimetallic catalyst for high-temperature PEM fuel cell to improve CO tolerance. International Journal of Energy Research 45 (2):3343–57. doi: 10.1002/er.6032 .
3. Alegre, C., L. Alvarez-Manuel, R. Mustata, L. Valiño, A. Lozano, and F. Barreras. 2019. Assessment of the durability of low-cost Al bipolar plates for High Temperature PEM fuel cells. International Journal of Hydrogen Energy 44 (25):12748–59. doi: 10.1016/j.ijhydene.2018.07.070 .
4. Authayanun, S., and V. Hacker. 2018. Energy and exergy analyses of a stand-alone HT-PEMFC based trigeneration system for residential applications. Energy Conversion and Management 160:230–42. doi: 10.1016/j.enconman.2018. 01.022 . Bell, I. H., J. Wronski, S. Quoilin, and V. Lemort. 2014. Pure and pseudo-pure fluid thermophysical property evaluation and the open-source thermophysical property library CoolProp. Industrial & Engineering Chemistry Research 53 (6):2498–508. doi: 10.1021/ie4033999
5. Chandan, A., M. Hattenberger, A. El-Kharouf, S. Du, A. Dhir, V. Self, B. G. Pollet, A. Ingram, and W. Bujalski. 2013. High temperature (HT) polymer electrolyte membrane fuel cells (PEMFC)–A review. Journal of Power Sources 231:264–78. doi: 10.1016/j.jpowsour.2012.11.126 .
6. Chen, Q., J. Xu, and H. Chen. 2012. A new design method for Organic Rankine Cycles with constraint of inlet and outlet heat carrier fluid temperatures coupling with the heat source. Applied Energy 98:562–73. doi: 10.1016/j.apenergy. 2012.04.035 .
7. Chen, Z., B. Yin, Z. Wei, and F. Dong. 2024. Coupling of high-temperature proton exchange membrane fuel cells with methanol steam reforming: Modeling and simulation for an integrated coupled for power generation system. Energy Conversion and Management 301:118044. doi: 10.1016/j.enconman.2023.118044 . Dirkes, S., J. Leidig, P. Fisch, and S. Pischinger. 2023. Prescriptive lifetime management for PEM fuel cell systems in transportation applications, Part I: State of the art and conceptual design. Energy Conversion and Management 277:116598. doi: 10.1016/j.enconman.2022.116598 .
8. Gomri, R., and R. Hakimi. 2008. Second law analysis of double effect vapour absorption cooler system. Energy Conversion and Management 49 (11):3343–48. doi: 10.1016/j.enconman.2007.09.033 .

9. Guo, F., X. Xiu, C. Li, K. Cheng, and J. Qin. 2023. Performance evaluation and off-design strategy of a high temperature proton exchange membrane fuel cell turbine-less hybrid system for low pressure ratio and Mach number aircraft. Journal of Power Sources 562:232752. doi: 10.1016/j.jpowsour.2023.232752 . Haghghi, M. A., M. Shamsaiee, S. Ghazanfari Holagh, A. Chitsaz, and M. A. Rosen. 2019. Thermodynamic, exergoe conomic, and environmental evaluation of a new multi-generation system driven by a molten carbonate fuel cell for production of cooling, heating, electricity, and freshwater. Energy Conversion and Management 199:112040. doi: 10. 1016/j.enconman.2019.112040 .

10. Hao, S. 2024. The technical and industrial challenges faced by fuel cells—A case study of PEMFC and SOFC. Highlights in Science, Engineering and Technology 81:607–14. doi: 10.54097/k3tbdx94 .

11. Kiani-Moghaddam, M., M. Shivaie, P. D. Weinsier, M. Kiani-Moghaddam, M. Shivaie, and P. D. Weinsier. 2019. Introduction to multi-objective optimization and decision-making analysis. Modern Music-Inspired Optimization Algorithms for Electric Power Systems: Modeling, Analysis and Practice 21–45.

12. Kiwan, S., and M. I. Radaideh. 2020. Investigation of a new hybrid fuel cell–ThermoElectric generator–absorption chiller system for combined power and cooling. International Journal of Refrigeration 113:103–14. doi: 10.1016/j.ijrefrig. 2020.02.010 .

13. Korsgaard, A. R., M. Pagh Nielsen, M. Bang, and S. Knudsen Kær. 2006. Modeling of CO influence in PBI electrolyte PEM fuel cells. In Paper presented at the International Conference on Fuel Cell Science, California, USA: Engineering and Technology.

14. Li, Y., D. Li, Z. Ma, M. Zheng, Z. Lu, H. Song, X. Guo, and W. Shao. 2022. Performance analysis and optimization of a novel vehicular power system based on HT-PEMFC integrated methanol steam reforming and ORC. Energy (Oxford) 257:124729. doi: 10.1016/j.energy.2022.124729 .

15. Ma, Z., L. Cai, X. Zhang, and X. Zhang. 2023. Thermodynamics and 3E analyses of a high-temperature proton exchange membrane fuel cell-based CCHP system with cascade utilization of waste heat. International Journal of Refrigeration 152:204–13. doi: 10.1016/j.ijrefrig.2023.04.027 .

16. Ma, Z., W. Wu, L. Sun, X. Zhang, X. Zhang, and L. Cai. 2024. Tri-generation design and analysis of methanol-reforming high-temperature fuel cell based on double-effect absorption cooling power cycle. Energy Conversion and Management 307:118379. doi: 10.1016/j.enconman.2024.118379 .

17. Mamaghani, A. H., B. Najafi, A. Casalegno, and F. Rinaldi. 2018. Optimization of an HT-PEM fuel cell based residential micro combined heat and power system: A multi-objective approach. Journal of Cleaner Production 180:126–38. doi: 10.1016/j.jclepro.2018.01.124 .

18. Marandi, S., N. Sarabchi, and M. Yari. 2021. Exergy and exergoeconomic comparison between multiple novel combined systems based on proton exchange membrane fuel cells integrated with organic Rankine cycles, and hydrogen boil-off gas subsystem. Energy Conversion and Management 244:114532. doi: 10.1016/j.enconman.2021.114532 .

19. Nalbant, Y., C. Ozgur Colpan, and Y. Devrim. 2020. Energy and exergy performance assessments of a high temperature-proton exchange membrane fuel cell based integrated cogeneration system. International Journal of Hydrogen Energy 45 (5):3584–94. doi: 10.1016/j.ijhydene.2019.01.252 .

20. Panahizadeh, F., M. Hamzehei, M. Farzaneh-Gord, and A. A. V. Ochoa. 2021. Energy, exergy, economic analysis and optimization of single-effect absorption chiller network. Journal of Thermal Analysis and Calorimetry 145 (3):669–99. doi: 10.1007/s10973-020-09966-4 .

21. Panchenko, V. A., Y. V. Daus, A. A. Kovalev, I. V. Yudaev, and Y. V. Litti. 2023. Prospects for the production of green hydrogen: Review of countries with high potential. International Journal of Hydrogen Energy 48 (12):4551–71. doi: 10. 1016/j.ijhydene.2022.10.084 .

22. Pátek, J., and J. Klomfar. 2006. A computationally effective formulation of the thermodynamic properties of LiBr–H2O solutions from 273 to 500 K over full composition range. International Journal of Refrigeration 29 (4):566–78. doi: 10. 1016/j.ijrefrig.2005.10.007 .

23. Patel, S., and K. K. Pant. 2006. Production of hydrogen with low carbon monoxide formation via catalytic steam reforming of methanol. Journal of Fuel Cell Science and Technology 3 (4):369–74. doi: 10.1115/1.2349514

24. Qureshi, F., F. Ahmad, M. Idrees, A. Asif Khan, and S. Zaidi. 2021. Simulation of methanol steam reforming process for the production of hydrogen. Indian Chemical Engineer 63 (1):99–116. doi: 10.1080/00194506.2019.1689186 . Restelli, F., E. Spatolisano, L. A. Pellegrini, A. R. De Angelis, S. Cattaneo, and E. Roccaro. 2024. Detailed techno-economic assessment of ammonia as green H2 carrier. International Journal of Hydrogen Energy 52:532–47. doi: 10.1016/j.ijhydene.2023.06.206 .

25. Sarabchi, N., S. M. Seyed Mahmoudi, M. Yari, and A. Farzi. 2019. Exergoeconomic analysis and optimization of a novel hybrid cogeneration system: High-temperature proton exchange membrane fuel cell/Kalina cycle, driven by solar energy. Energy Conversion and Management 190:14–33. doi: 10.1016/j.enconman.2019.03.037 .

26. Sarabchi, N., M. Yari, and S. M. Seyed Mahmoudi. 2021. Exergy and exergoeconomic analyses of novel high-temperature proton exchange membrane fuel cell based combined cogeneration cycles, including methanol steam reformer integrated with catalytic combustor or parabolic trough solar collector. Journal of Power Sources 485:229277. doi: 10.1016/j.jpowsour.2020.229277 .

27. Simon Araya, S., V. Liso, X. Cui, N. Li, J. Zhu, S. L. Sahlin, S. H. Jensen, M. P. Nielsen, and S. K. Kær. 2020. A review of the methanol economy: The fuel cell route. Energies (Basel) 13 (3):596. doi: 10.3390/en13030596 .

28. Singh, U. R., S. Bhogilla, and J.-K. Kuo. 2024. A novel thermally integrated high-temperature PEM fuel cell and absorption system for sustainable heating/cooling application. International Journal of Hydrogen Energy. doi: 10. 1016/j.ijhydene.2024.03.336.

29. Villafana, E. D. S., and J. Pablo Vargas Machuca Bueno. 2019. Thermoeconomic and environmental analysis and optimization of the supercritical CO2 cycle integration in a simple cycle power plant. Applied Thermal Engineering 152:1–12. doi: 10.1016/j.applthermaleng.2019.02.052 .

30. Wagner, W., and A. Pruß. 2002. The IAPWS formulation 1995 for the thermodynamic properties of ordinary water substance for general and scientific use. Journal of Physical & Chemical Reference Data 31 (2):387–535. doi: 10.1063/1. 1461829 .

31. Wu, W., C. Zhai, Y. Sui, and H. Zhang. 2021. A novel distributed energy system using high-temperature proton exchange membrane fuel cell integrated with hybrid-energy heat pump. Energy Conversion and Management 235:113990. doi: 10.1016/j.enconman.2021.113990 .

32. Xiao, S., X. Xu, J. Xu, and X. Xu. 2024. Operating performance characteristics and analysis of a high temperature fuel cell system integrated with a methanol steam reformer. International Journal of Hydrogen Energy 50:1200–17. doi: 10. 1016/j.ijhydene.2023.06.233.

33. Xie, N., Z. Xiao, W. Du, C. Deng, Z. Liu, and S. Yang. 2023. Thermodynamic and exergoeconomic analysis of a proton exchange membrane fuel cell/absorption chiller CCHP system based on biomass gasification. Energy (Oxford) 262:125595. doi: 10.1016/j.energy.2022.125595 .

34. Xing, S., C. Zhao, S. Ban, Y. Liu, and H. Wang. 2020. Thermodynamic performance analysis of the influence of multi-factor coupling on the methanol steam reforming reaction. International Journal of Hydrogen Energy 45 (11):7015–24. doi: 10.1016/j.ijhydene.2019.12.192 .

35. Yang, Y., H. Zhang, P. Yan, and K. Jermsittiparsert. 2020. Multi-objective optimization for efficient modeling and improvement of the high temperature PEM fuel cell based Micro-chp system. International Journal of Hydrogen Energy 45 (11):6970–81. doi: 10.1016/j.ijhydene.2019.12.189 .

36. Yuan, Y., L. Chen, X. Lyu, W. Ning, W. Liu, and W.-Q. Tao. 2024. Modeling and optimization of a residential pemfc-based CHP system under different operating modes. Applied Energy 353:122066. doi: 10.1016/j.apenergy. 2023.122066 .

37. Zhu, J., S. Simon Araya, X. Cui, S. Lennart Sahlin, and S. Knudsen Kær. 2020. Modeling and design of a multi-tubular packed-bed reactor for methanol steam reforming over a Cu/ZnO/Al2O3 catalyst. Energies (Basel) 13 (3):610. doi: 10.